Rapid microbial interaction network inference in microfluidic droplets

Ryan H. Hsu[1], Ryan L. Clark[1], Jin Wen Tan[1], Philip A. Romero[1,3] & Ophelia S. Venturelli[1,2,3]*

[1]Department of Biochemistry, University of Wisconsin-Madison, Madison, WI 53706

[2]Department of Bacteriology, University of Wisconsin-Madison, Madison, WI 53706

[3]Department of Chemical & Biological Engineering, University of Wisconsin-Madison, Madison, WI 53706

*To whom correspondence should be addressed: venturelli@wisc.edu

ABSTRACT

Microbial interactions are major drivers of microbial community dynamics and functions. However, microbial interactions are challenging to decipher due to limitations in parallel culturing of sub-communities across many environments and accurate absolute abundance quantification of constituent members of the consortium. To this end, we developed Microbial Interaction Network Inference in microdroplets (MINI-Drop), a high-throughput method to rapidly infer microbial interactions in microbial consortia in microfluidic droplets. Fluorescence microscopy coupled to automated computational droplet and cell detection was used to rapidly determine the absolute abundance of each strain in hundreds to thousands of droplets per experiment. We show that MINI-Drop can accurately infer pairwise as well as higher-order interactions using a microbial interaction toolbox of defined microbial interactions mediated by distinct molecular mechanisms. MINI-Drop was used to investigate how the molecular composition of the environment alters the interaction network of a three-member consortium. To provide insight into the variation in community states across droplets, we developed a probabilistic model of cell growth modified by microbial interactions. In sum, we demonstrate a robust and generalizable method to probe cellular interaction networks by random encapsulation of sub-communities into microfluidic droplets.

INTRODUCTION

Microbial communities have a tremendous impact on diverse environments ranging from the human body to the plant rhizosphere (Berendsen et al., 2012; Clemente et al., 2012). Microbe-microbe and environment-microbe interactions are major determinants of microbial communities and microbiomes (Cao et al., 2018; Venturelli et al., 2016). Deciphering interaction networks in high-dimensional microbial communities is challenging due to the need to rapidly and accurately determine the absolute abundance of each community member across many sub-communities and environments (Cao et al., 2017; Harcombe et al., 2016).

The population sizes of microbial consortia can range from less than ten cells in mixed species biofilm aggregates to 10^{11} cells mL^{-1} in the human colon (Connell et al., 2014; Sender et al., 2016; Stoodley et al., 2001). Cellular growth history, the temporal order of strain colonization or the initial phase of microbial competition can impact community assembly (von Bronk et al., 2017; Kong et al., 2018; Vega and Gore, 2017; Venturelli et al., 2018; Zhou et al., 2013). Our understanding of microbial consortia in small populations is limited due to technical challenges in the manipulation and analysis of small populations of cells (Connell et al., 2014). Therefore, high-throughput methods that can rapidly resolve microbial interaction networks across different initial community states, population sizes and environments would enable a better understanding of the key parameters shaping the structure and function of microbial communities and how to harness these systems for diverse biotechnological applications.

Microbial interaction network inference requires accurate measurements of the absolute abundance of each member of the community (Fisher and Mehta, 2014). Recent experimental efforts have used models trained on measurements of 1-3 member communities to predict community composition or function of up to 12 members to varying degrees of accuracy (Friedman et al., 2017; Guo and Boedicker, 2016; Kong et al., 2018; Mounier et al., 2008; Venturelli et al., 2018). Absolute abundance quantification of each member of a microbial community has ranged from low-throughput selective plating to count colony forming units (tens of samples per experiment) (Mounier et al., 2008) to optical density multiplied by relative abundance based on next-generation sequencing of samples generated through robotic high-throughput culturing (hundreds of samples per experiment) (Venturelli et al., 2018).

47   Encapsulation of microbial communities into microdroplets has been used to study
48 ecological and evolutionary processes of microbial communities (Bachmann et al., 2013; Park et
49 al., 2011). Water-in-oil droplets can be generated at kilohertz (kHz) rates using microfluidics,
50 wherein cells from a mixed culture are randomly encapsulated into droplets yielding diverse sub-
51 communities that can be studied in parallel (millions of samples per experiment). Each droplet is
52 a miniaturized compartment that can be used to study interactions between community members
53 in small populations. Microfluidic technologies enable the generation of well-controlled droplet
54 environments of ~1% size variation (Guo et al., 2012). However, previous studies have not fully
55 leveraged the capabilities of this technology to quantitatively investigate microbial communities.
56 Further, we lack a systematic method to rapidly infer microbial interactions using droplet
57 microfluidics in different environmental contexts.

58   To address this challenge, we developed Microbial Interaction Network Inference in
59 Droplets (MINI-Drop). To determine the absolute abundance of each strain across hundreds to
60 thousands of samples, we developed an automated computational method coupled to
61 fluorescence microscopy to rapidly segment droplet images and accurately count fluorescently
62 labeled cells within each droplet. We tested the capability of MINI-Drop to accurately infer
63 microbial interactions using a microbial interaction toolbox composed of positive and negative
64 interactions mediated by distinct molecular mechanisms. Our results demonstrate that MINI-Drop
65 can accurately decipher pairwise as well as higher-order interactions by analyzing droplets
66 containing 1-3 strains. We investigated how the molecular composition of the environment shapes
67 the ecological network of a three-member consortium. A probabilistic model of cell growth
68 modified by microbial interactions and cell death described the variability in community states
69 across droplets containing the same initial strain composition, providing insight into the forces
70 shaping community assembly in small populations.

71 **RESULTS**

72

73 *Inferring microbial interactions in microfluidic droplets*
74 Microbial interactions represent the net impact (positive, negative or negligible) of an organism
75 on the growth of another over a specified time interval (Cao et al., 2018). Microbial interactions
76 can be quantified by evaluating the difference in phenotype (e.g. growth response or metabolic
77 activity) of an organism in the absence and presence of another strain (partner strain).
78 Encapsulation of cells in a microbial community into droplets using techniques from droplet-
79 microfluidics enables parallel culturing of many sub-communities (**Fig. 1a**). To infer microbial
80 interactions, we needed a scalable method to determine the absolute abundance of each strain
81 within each droplet. The average fluorescence in each droplet was not proportional to the number
82 of cells due to variability in cellular growth rates, which dictates the rate of dilution of the
83 fluorescent reporter (**Fig. S1a**). Therefore, we developed an automated procedure using
84 techniques from computer vision to rapidly identify droplets (**Fig. S1b**) and count the number of
85 fluorescently labeled cells in each droplet (**Fig. S1c**). The droplets were binned according to strain
86 composition (**Fig. S1d)** and the cell counts were used to infer interaction type (positive, negative
87 or negligible), strength and directionality (see Materials and Methods).

88   To evaluate the accuracy and dynamic range of the method, CFP-labeled *E. coli*, RFP-
89 labeled *E. coli* and YFP-labeled *S. typhimurium* were mixed in equal volumetric ratios and serially
90 diluted to generate a broad range of cell densities (**Fig. 1b**). Each dilution of the mixed culture
91 was encapsulated into 34 picoliter (pL) droplets (40 µm diameter), imaged using fluorescence

92 microscopy, and analyzed using a computational workflow (see Materials and Methods). The
93 number of cells of each fluorescently labeled strain decreased linearly with each dilution, with the
94 exception of the highest density droplets (**Fig. 1c, Fig. S2a**). These data demonstrate at least a
95 64-fold linear range of the cell counting method of each fluorescent reporter. In a separate
96 experiment involving growth of fluorescently labeled strains in droplets described below (**Table 1**,
97 E6), droplet size did not correlate with the number of cells labeled with CFP, YFP or RFP,
98 indicating that variation in droplet size did not contribute to variability in cell growth (**Fig. S2b,c,d**).

99
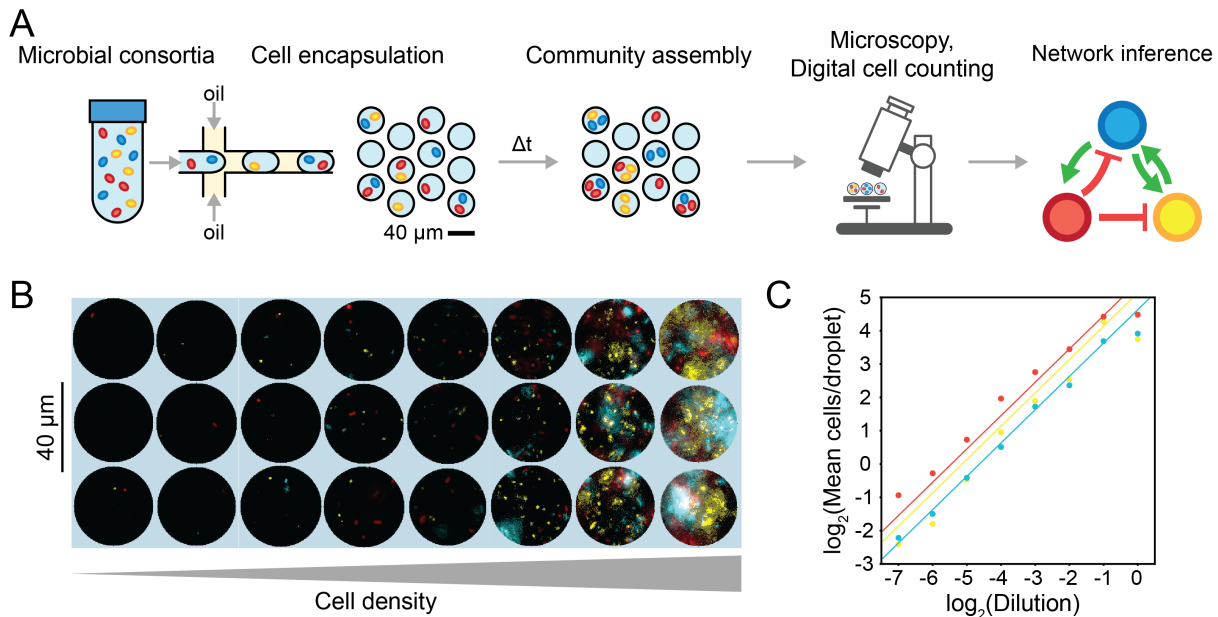
100

101 **Fig. 1. Overview and characterization of microbial interaction network inference in microdroplets**
102 **(MINI-Drop). (a)** Overview schematic of the MINI-Drop method. A mixed microbial culture and oil are loaded
103 into a droplet-forming microfluidic device. Cells are randomly encapsulated into droplets based on a Poisson
104 distribution. The droplets are incubated for a period of time to allow cell growth and division and then imaged
105 using fluorescent microscopy. A computer vision workflow rapidly identifies droplets and determines the
106 number of each fluorescently labeled strain within each droplet (**Fig. S1**). A microbial interaction network is
107 inferred based on the difference in the mean number of cells in the absence and presence of a partner
108 strain. **(b)** Representative fluorescent microscopy images of droplets containing three bacterial strains
109 labeled with YFP (ST Lac*), RFP (EC WT) or CFP (EC Met-) (see **Table 2**). **(c)** Scatter plot of the dilution
110 factor of the mixed culture vs. the $\log_2$ transform of the mean number of cells per drop (**Fig. S2a**). Each
111 data point represents the mean of 400-600 droplets and lines denote linear regression fits to the data. Red,
112 yellow and blue data points correspond to EC WT, ST Lac* and EC Met-, respectively.

113

Investigating microbial interaction networks two-member consortia
115 To determine whether MINI-Drop could illuminate microbial interactions in microbial consortia, we
116 investigated two-member consortia engineered to display defined interactions. A microbial
117 interaction was defined as a statistically significant difference in the average number of cells of a
118 given strain in the presence of a second strain (partner) compared to the absence of the partner
119 at a specific time point. To investigate positive interaction networks with MINI-Drop, we
120 constructed a consortium composed of an RFP-labeled *E. coli* methionine auxotroph (EC Met-)

4

121　and a GFP-labeled *B. subtilis* tryptophan auxotroph (BS Trp-, **Table 1**, E1). In the absence of
122　supplemented amino acids, the growth of *B. subtilis* requires secretion of tryptophan from *E. coli*
123　and the growth of *E. coli* requires secretion of methionine from *B. subtilis*, which together
124　generates a bidirectional positive interaction network (**Fig. 2a**). The two species were mixed in
125　equal proportions based on OD600 measurements, encapsulated into droplets such that each
126　droplet had 1-2 cells on average according to a Poisson distribution and the droplets were
127　incubated at 37°C for 18 hours. The fluorescence microscopy images demonstrated that single
128　species droplets exhibited a low number of total cells, whereas droplets containing both species
129　exhibited significantly higher number of cells of each strain (**Fig. 2b**). Specifically, the average
130　number of EC Met- cells was 3.3-fold (p = 3.8e-26) higher in the presence of BS Trp- compared
131　to the average number of EC Met- in single-species droplets (**Fig. 2c**). Similarly, the average
132　number of BS Trp- cells was 4.2-fold (p = 1.5e-6) higher in the presence of EC Met- compared to
133　the average number of BS Trp- cells in single-species droplets (**Fig. 2c**). The inferred interaction
134　network exhibited bidirectional positive interactions, mirroring the topology of the expected
135　interaction network (**Fig. 2a,d**), demonstrating that MINI-Drop could deduce positive interactions.
136　Corroborating this result, the cell counts for BS Trp- and EC Met- were positively correlated (**Fig.
137　S3a**).

138　　　　We next investigated whether MINI-Drop could decipher negative interactions. A synthetic
139　community was constructed wherein a GFP-labeled *E. coli* strain (sender strain) was engineered
140　to express LuxI, a synthetase for the quorum-sensing signal C6 acyl homoserine lactone (AHL).
141　AHL diffuses into the RFP-labeled *E. coli* strain (receiver strain), binds and activates the receptor
142　LuxR, which regulates the expression of the MazF toxin (**Fig. 2e**, **Table 1**, E2). High expression
143　levels of the endoribonuclease MazF inhibits cell growth by inducing mRNA decay (Venturelli et
144　al., 2017), generating a strong negative interaction from the sender to the receiver. To
145　characterize this community using MINI-Drop, the sender and receiver strains were mixed in equal
146　proportions based on OD600, encapsulated into droplets and incubated at 37°C for 18 hr.
147　Computational analysis of the fluorescent microscopy images showed that the number of receiver
148　cells was significantly lower in droplets containing both the sender and receiver strains compared
149　to the average number of receiver cells in single-strain droplets (**Fig. 2f**). The average number of
150　receiver cells in the presence of the sender was 2.6-fold lower (p = 3.7e-14) compared to the
151　average number of receiver cells in droplets containing the receiver strain alone (**Fig. 2g**). In
152　addition, the average number of sender cells was 1.25-fold lower (p = 2.2e-4) in the presence of
153　the receiver compared to in its absence (**Fig. 2g**). The average number of sender cells in droplets
154　containing the sender strain alone was 16.7-fold higher than the average number of receiver cells
155　in droplets containing only the receiver strain, presumably due to leakiness of *mazF* from the pLux
156　promoter in the absence of AHL. Based on these data, the inferred interaction network exhibited
157　a strong negative interaction from the sender to the receiver and a weak negative interaction from
158　the receiver to the sender (**Fig. 2h**). The cell counts of the sender and receiver were negatively
159　correlated across droplets, corroborating the presence of negative interactions (**Fig. S3b**). In sum,
160　these data demonstrate that MINI-Drop can decipher negative interactions in microbial consortia.

161
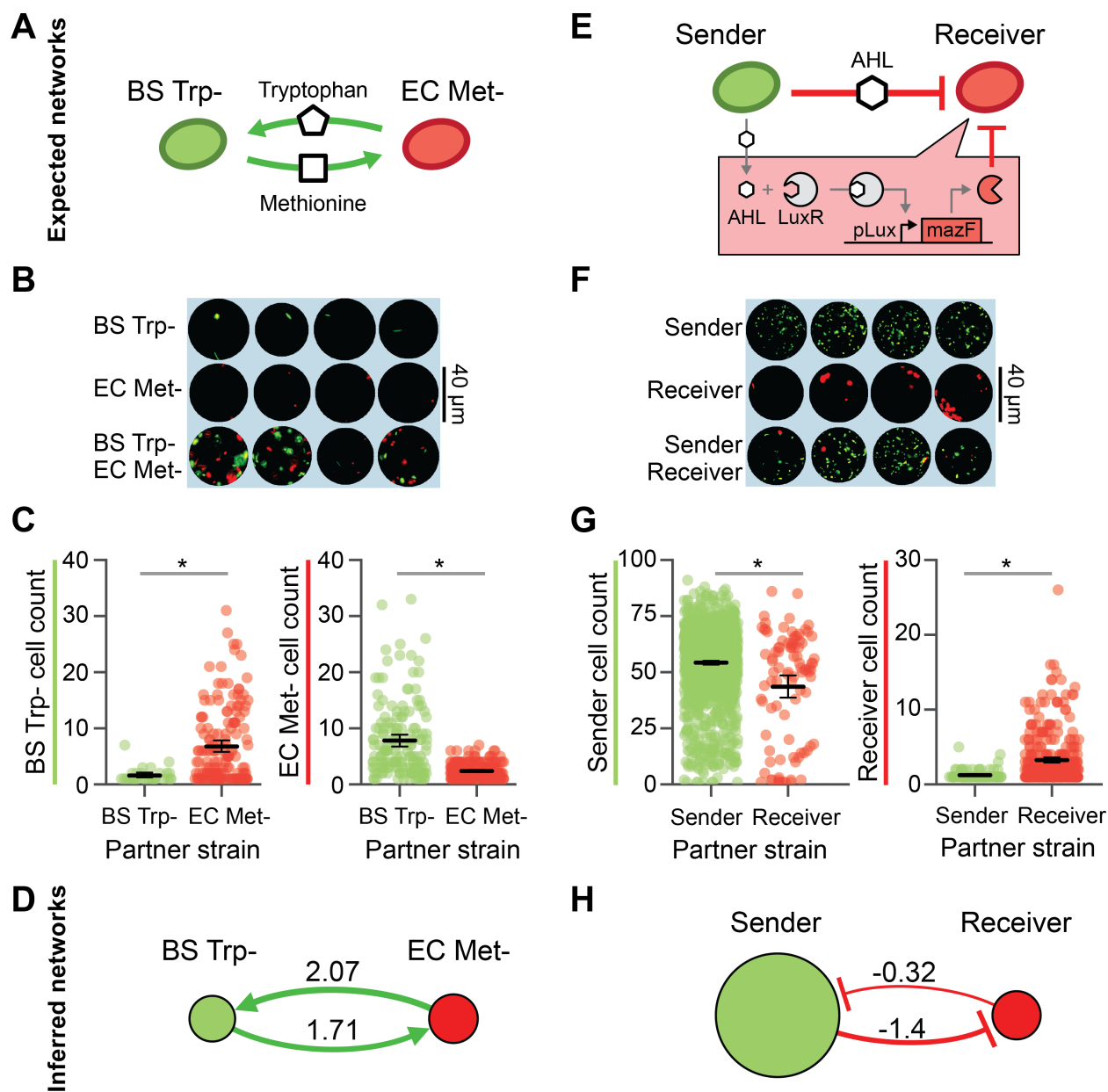
Fig. 2. Investigating positive and negative microbial interaction networks using MINI-Drop. (a) Schematic of the expected network for a synthetic consortium composed of an RFP-labeled *E. coli* methionine auxotroph (EC Met-) and a GFP-labeled *B. subtilis* tryptophan auxotroph (BS Trp-) (**Table 1**, E1). **(b)** Fluorescence microscopy image of representative single-species (EC Met- or BS Trp-) or two-member droplets. **(c)** Categorical scatter plot showing the number of BS Trp- or EC Met- cells in each droplet. The black horizontal line represents the mean and the error bars denote bootstrapped 95% confidence intervals for the mean. Gray lines denote statistically significant difference in means based on the Mann-Whitney U test (n=87, p=1.5e-6, left and n=372, p=3.8e-26, right). **(d)** The inferred interaction network for the EC Met-, BS Trp- consortium. The edge width is proportional to the log$_2$ ratio of the average cell count in the presence of a partner to the average cell count in single strain droplets. Node size is proportional to the average cell count of each strain in single strain droplets. **(e)** Schematic of the expected network of an *E. coli* community that exhibits a strong unidirectional negative interaction. A GFP-labeled strain (sender) expresses LuxI, a synthetase for the quorum-sensing signal C6 acyl homoserine lactone (AHL). AHL binds to the receptor LuxR in an RFP-labeled strain (receiver) and activates the expression of

6

177   a toxin MazF, generating a strong negative interaction (**Table 1**, E2). **(f)** Fluorescence microscopy image
178   of representative droplets containing the sender strain, receiver strain or community. **(g)** Categorical scatter
179   plot of the number of sender or receiver cells in each droplet in the presence or absence of a partner. The
180   black line represents the mean and the error bars denote bootstrapped 95% confidence intervals for the
181   mean. Gray lines denote statistically significant differences in the means (n=1512, p=2.2e-4, left, n=421,
182   p=3.8e-14, right). **(h)** The inferred interaction network for the mazF inhibition consortium.

183

184   *The molecular composition of the environment shapes a microbial interaction network*
185   The molecular composition of the environment influences the energetic costs and benefits of
186   microbial interactions in microbial communities (Cao et al., 2018; Harcombe et al., 2016; Liu et
187   al., 2017). A key challenge is predicting how the microbial interaction network is modulated by
188   environmental parameters. To investigate this question, we constructed a three-member
189   community consisting of two strains interacting via bidirectional positive interactions and a third
190   strain that promoted growth of constituent members of the community but did not receive a benefit
191   from the community. Specifically, the strains included RFP-labeled *E. coli* (EC WT), CFP-labeled
192   *E. coli* methionine auxotroph (EC Met-), and YFP-labeled *S. typhimurium* (ST Lac-). This
193   consortium was characterized in four conditions that varied the carbon source (lactose or glucose)
194   and the presence or absence of supplemented methionine. In lactose minimal media, *E. coli* can
195   consume lactose and secrete carbon byproducts that can be utilized as substrates by ST Lac*
196   (**Table 1**, E3-6) (Harcombe, 2010). In the absence of supplemented methionine, the growth of EC
197   Met- is dependent on methionine provided by constituent community members.
198   We used MINI-Drop to infer the pairwise microbial interaction network based on the
199   patterns in the number of cells of each community member in single strain and two-member
200   droplets. In lactose minimal media lacking supplemented methionine, the inferred network
201   recapitulated the expected network, exhibiting bidirectional positive interactions between ST Lac*
202   and EC Met- and unidirectional positive interactions from EC WT to ST Lac* to EC Met- (**Fig.
203   3a,e,i, Table 1**, E3, **Table S1**). In lactose minimal media supplemented with methionine, the
204   positive outgoing interactions from EC WT or ST Lac* to EC Met- were absent in the network and
205   bidirectional negative interactions linked EC Met- and EC WT (**Fig. 3b,f,j, Table 1**, E4). In glucose
206   minimal media lacking supplemented methionine, the positive interactions from EC WT or EC
207   Met- to ST Lac* were absent and instead EC WT and ST Lac* were coupled by bidirectional
208   negative interactions (**Fig. 3c,g,k, Table 1**, E5). By contrast to the expected network, bidirectional
209   negative interactions were inferred between all pairs of strains in glucose minimal media
210   supplemented with methionine (**Fig. 3d,h,l, Table 1**, E6). Across all conditions, the sign of the
211   Pearson correlation coefficient clustered according to the pairwise network topology, wherein
212   positive or negative correlation coefficients were associated with positive or negative interactions,
213   respectively (**Fig. S3, Fig. S4**). These data show that correlations in the absolute abundance of
214   strains across droplets can be used to classify specific topologies of two-member microbial
215   interaction networks. Media containing lactose as a primary carbon source promoted strain co-
216   existence in three-member droplets, suggesting that positive interactions from EC Met- or EC WT
217   to ST Lac* are critical interactions that promote community stability across different environments
218   (**Fig. S5a**). In sum, our results demonstrate that the microbial interaction network is highly context-
219   dependent and the network topology changes as a function of the molecular composition of the
220   environment.
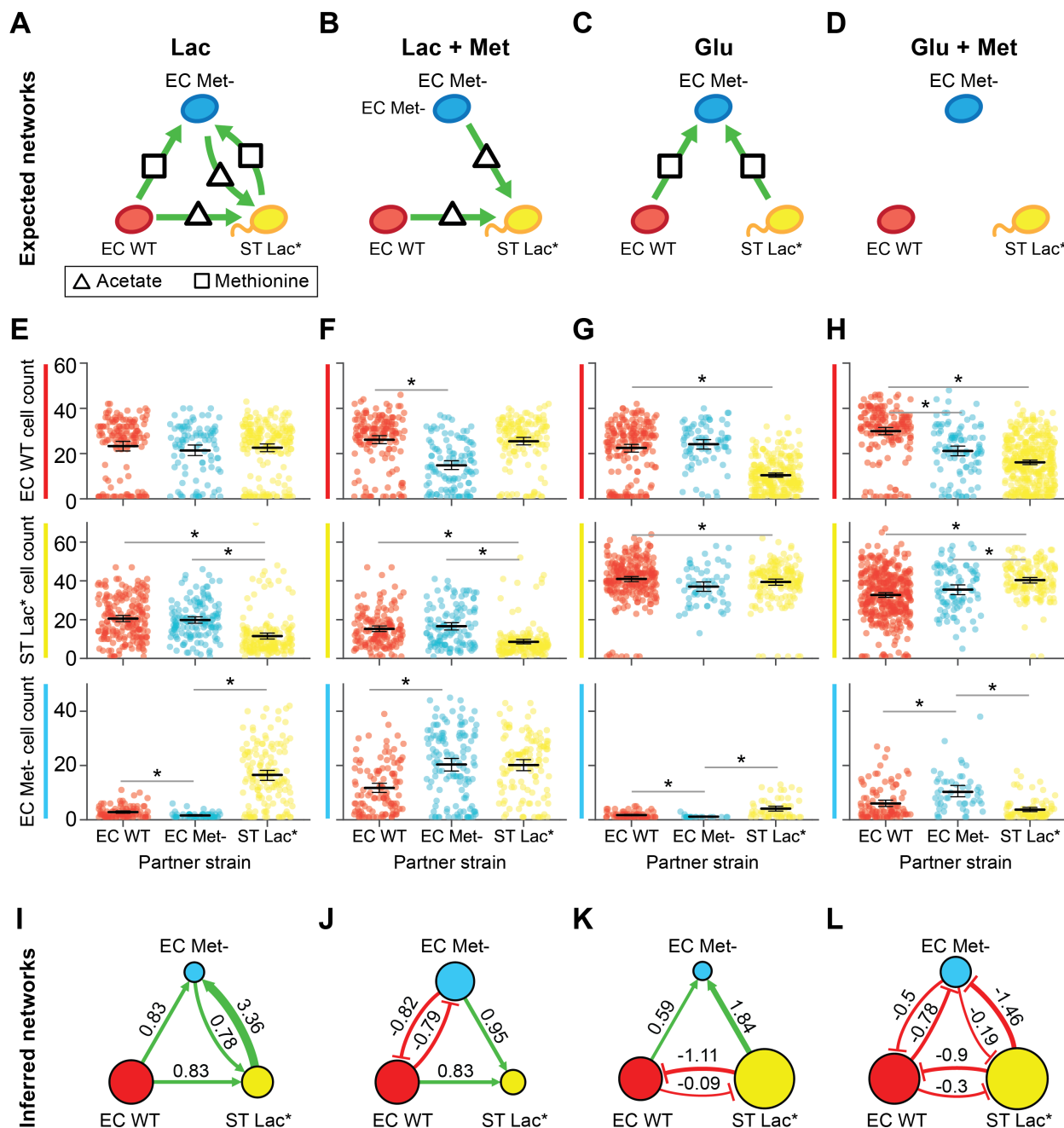
Fig. 3. The molecular composition of the environment shapes the interaction network of a three-member consortium. (a) Schematic of the expected microbial interaction network of a three-member consortium consisting of RFP-labeled *E. coli* (EC WT), CFP-labeled *E. coli* methionine auxotroph (EC Met-), and YFP-labeled *S. Typhimurium* deficient in lactose metabolism (ST Lac*) in lactose minimal media lacking supplemented methionine (**Table 1,** E3). Secreted carbon byproducts (acetate) and methionine are represented by a triangle and rectangle, respectively. Node colors and green arrows denote the type of fluorescent reporter and positive interactions, respectively. **(b)** Schematic of the expected microbial interaction network in lactose minimal media supplemented with methionine (**Table 1**, E4). **(c)** Schematic of the expected microbial interaction network in glucose minimal media lacking supplemented methionine (**Table 1**, E5). **(d)** Schematic of the expected microbial interaction network in glucose minimal media supplemented with methionine (**Table 1**, E6). **(e)** Cell count distributions in lactose minimal media for EC

233 WT (top), ST Lac* (middle) or EC Met- (bottom). The black line represents the mean and the error bars
234 denote the bootstrapped 95% confidence intervals for the mean. The gray horizontal bars indicate a
235 statistically significant difference (p < 0.05, **Table S1**) based on the Mann-Whitney U test. **(f)** Cell count
236 distributions in lactose minimal media supplemented with methionine for EC WT (top), ST Lac* (middle) or
237 EC Met- (bottom). **(g)** Cell count distributions in glucose minimal media for EC WT (top), ST Lac* (middle)
238 or EC Met- (bottom). **(h)** Cell count distributions of EC WT (top), ST Lac* (middle) or EC Met- (bottom) in
239 glucose minimal media supplemented with methionine. **(i)** Inferred interaction network in lactose minimal
240 media lacking supplemented methionine. The edge width is proportional to the $\log_2$ ratio of the average cell
241 count in the presence of a partner to the average cell count in the absence of the partner. Node size is
242 proportional to the average cell count of each strain grown in isolation. **(j)** Inferred network in lactose minimal
243 media supplemented with methionine. **(k)** Inferred interaction network in glucose minimal media lacking
244 supplemented methionine. **(l)** Inferred interaction network in glucose minimal media supplemented with
245 methionine.

246

247 *Investigating higher-order interactions using MINI-Drop*
248 Higher-order interactions occur when a pairwise interaction is modified in the presence of a third
249 community member (Bairey et al., 2016; Society, 2015) and these interactions are challenging to
250 identify in microbial communities. In MINI-Drop, a higher-order interaction was defined as a
251 difference in the presence and sign (positive or negative) of an interaction in a three-member
252 community compared to the presence and sign of the interaction in each two-member sub-
253 community (**Fig. 4a**). We tested whether MINI-Drop could identify higher-order interactions by
254 analyzing the cell count distributions of each strain in three-member droplets in addition to single-
255 strain and two-member droplets. To do so, a community consisting of an RFP-labeled *E. coli*
256 methionine auxotroph that is also deficient in lactose metabolism (EC Met- Lac*, **Table 1**, E7),
257 EC Met- (CFP) and ST Lac* was constructed. In lactose minimal media lacking supplemented
258 methionine, EC Met- and ST Lac* can secrete carbon byproducts and methionine, respectively
259 and thus together enable the growth of EC Met- Lac*. Our results showed that the number of EC
260 Met- Lac* cells was higher in the presence of both EC Met- and ST Lac* but not in the presence
261 of either single strain, demonstrating that MINI-Drop could identify higher-order interactions (**Fig.**
262 **4b**, p=0.0012). The strains EC Met- (CFP) and ST Lac* interacted via bidirectional positive
263 interactions, recapitulating the expected network topology (**Fig. 3a**, **Fig. S5b,c**). In addition, the
264 cell counts of EC Met- and ST Lac* displayed a strong positive correlation (**Fig. S3d**).
265 　　　To investigate other higher-order interactions that were present in our data, we analyzed
266 droplets containing three-member consortium (EC WT, EC Met- and ST Lac), two-member sub-
267 communities and single strains across four different environments (**Fig. 3, Table 1**, E3-E7). Our
268 results illuminated a higher-order interaction in lactose minimal media (**Table 1**, E3), where EC
269 WT was significantly inhibited in the presence of both EC Met- and ST Lac*, while no negative
270 interaction was observed in the pairwise interaction networks of EC WT co-cultured with EC Met-
271 or ST Lac* (**Fig. 3a, 4d,e**). Unexpected higher-order interactions occurred in one of twelve
272 possible cases (3 community members times 4 environments) in the EC Met-, EC WT, ST Lac*
273 consortium (**Table 1**, E3-6**)**, In sum, our results show that MINI-Drop can rapidly elucidate higher-
274 order interactions based on the absolute abundance patterns in droplets containing 1-3 strains.
275 demonstrating that higher-order interactions were infrequent in this community across different
276 environmental conditions.
277 　　　To evaluate the sensitivity of the method, we next investigated the number of droplets
278 containing the same initial strain composition (replicates) required to infer microbial interactions
279 of different strengths across all datasets. Specifically, we analyzed the relationship between

280 interaction strength magnitude, number of replicates, and interaction significance ($p < 0.05$) in all
281 datasets (**Fig. S6**). Our results showed that the significance of each interaction increased
282 exponentially as a function of the number of droplets (**Fig. S6a**). The strength of the interaction
283 was inversely related to the number of droplets required for statistical significance of the
284 interaction. For example, strong interactions required as few as 15 replicates whereas weak
285 interactions required more than 50 replicates (**Fig. S6b**).

286
287
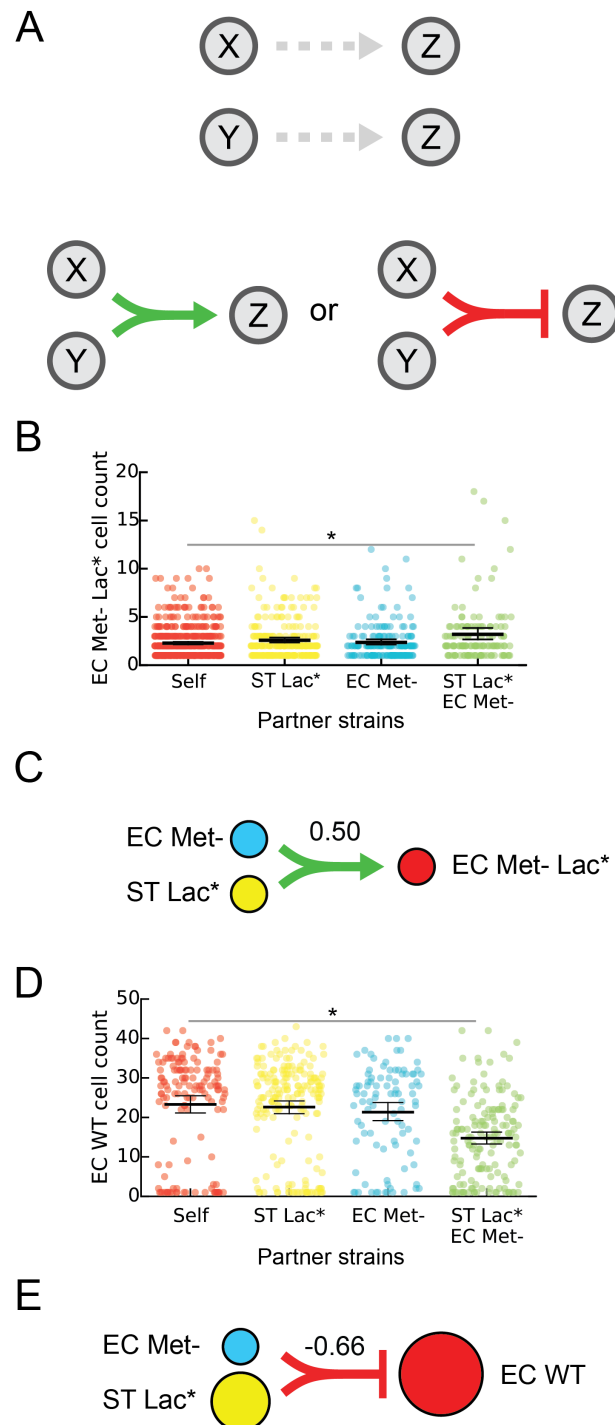
288

289 **Fig. 4. Investigating higher-order interactions using MINI-Drop. (a)** Schematic showing an example of
290 a higher-order interaction. Droplets containing two strains X and Z or Y and Z do not exhibit interactions. In
291 three-member droplets, a negative or positive interaction from X and Y to Z is present and is defined as a
292 higher-order interaction. **(b)** Categorical scatter plots of the number of EC Met- Lac* cells in droplets
293 containing the single strain EC Met- Lac* (self), pairs of strains including EC Met- Lac* and EC Met- or ST
294 Lac* or all three strains (EC Met- Lac*, EC Met- and ST Lac*). Black horizontal bars denote the mean
295 number of cells per droplet and error bars represent the bootstrapped 95% confidence interval for the mean.
296 The horizontal bar (gray) represents a statistically significant difference in means based on the Mann-
297 Whitney U test (p = 1.2e-3, n = 703). **(c)** Schematic showing the higher-order inferred network for the data
298 shown in panel (b). The line width represents the inferred strength of the higher-order interaction. Node size
299 is proportional to the average cell count of each strain grown in isolation. **(d)** Categorical scatter plots of the
300 number of EC WT cells in droplets containing the single strain EC WT, two strains including EC WT and ST
301 Lac* or EC Met- or all three strains (EC WT, ST Lac* and EC Met-) in lactose minimal media. The horizontal
302 bar (gray) represents a statistically significant difference in means based on the Mann-Whitney U test (p =
303 2.9e-10, n = 296). **(e)** Schematic showing a higher-order interaction inferred using the data shown in (d).
304 The line width represents the strength of the inferred higher-order interaction. Node size is proportional to
305 the average cell count of each strain grown in isolation.

306

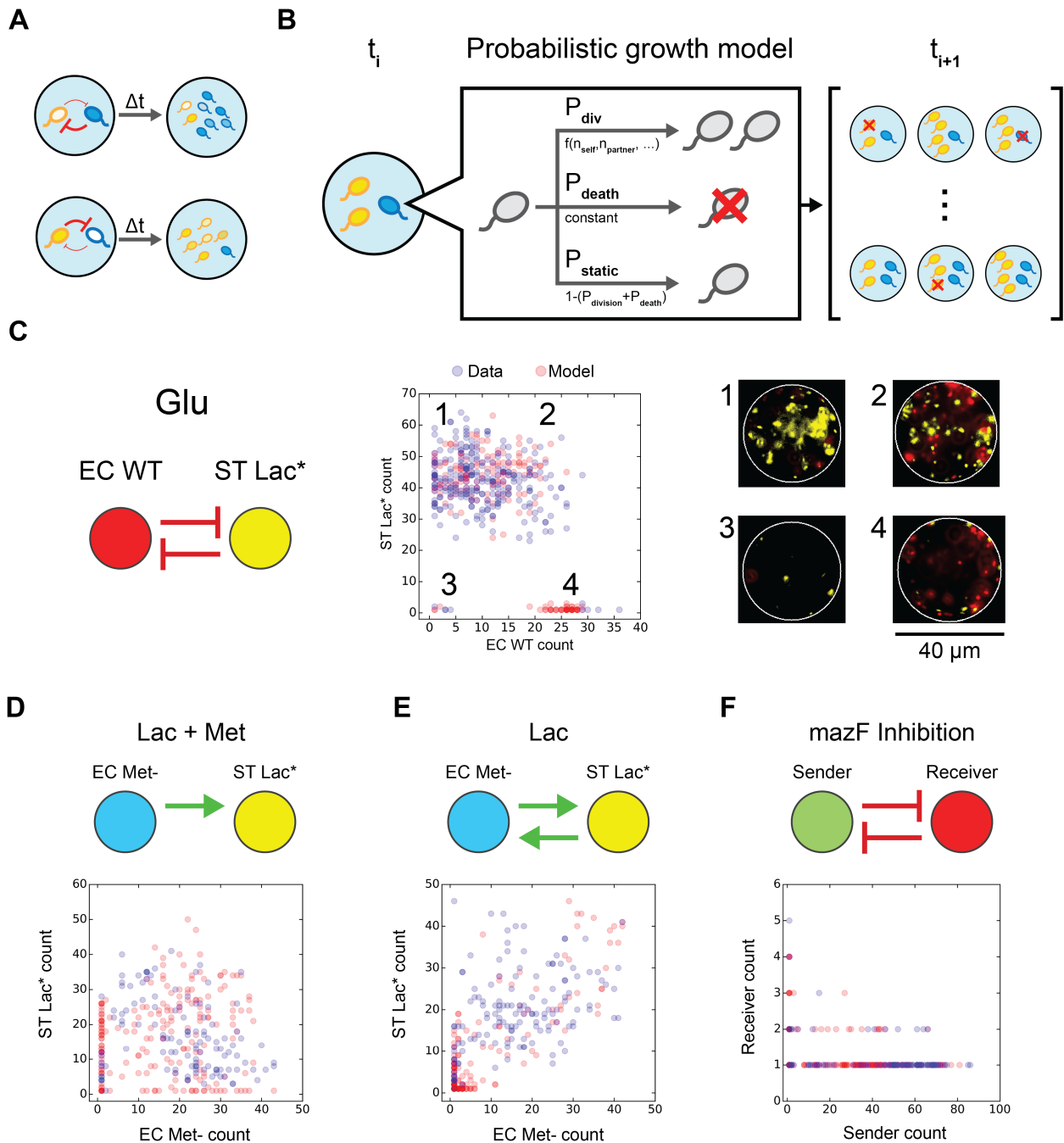307 *Discrete-time Markov model of community assembly*
308 In small microbial populations, stochastic variation in intracellular molecular concentrations,
309 growth and death can impact community assembly and functions (Boedicker et al., 2009; Connell
310 et al., 2014; Hansen et al., 2016). To model community assembly in small populations, microbial
311 growth can be represented as a probabilistic event, such that two communities seeded with the
312 same initial strain composition exhibit different steady-state community compositions (**Fig. 5a**)
313 (Horowitz et al., 2010). We constructed a discrete-time Markov model of cell growth modified by
314 microbial interactions to investigate the variability in community composition across droplets
315 containing the same initial strain composition.
316   In the model, communities are initially seeded with a single cell of each type. At each time
317 step, strain *i* can undergo cell division, death or remain static according to the probabilities $P_{div,i}$,
318 $P_{death,i}$, and $P_{static,i}$, respectively (**Fig. 5b**). The probabilities $P_{div,i}$ and $P_{static,i}$ are a function of
319 the number of cells of each strain with parameters specific to each strain and the probability
320 $P_{death,i}$ is a fixed parameter. Negative interactions with self or non-self are represented by inverted
321 sigmoidal logistic functions, such that the probability of cell division is inversely related to the cell
322 number. Positive interactions are represented as sigmoidal logistic functions, such that the
323 probability of cell division increases as a function of the number of partner cells (see Materials
324 and Methods).
325   We tested whether this modeling framework could recapitulate the experimental cell count
326 distributions, based on the assumption that the measurement time point maps to the steady-state
327 of the model. Models were constructed using the positive or negative interaction functions and
328 model parameters were identified to recapitulate the cell count distributions of each strain. We
329 constructed a model for the EC WT, ST Lac* community grown in glucose minimal media that
330 exhibited a bidirectional negative interaction network (**Fig. 5c**, left). Our results showed three
331 clusters representing distinct community states exhibiting high abundance of one strain (**Fig. 5c**,
332 center, clusters 1 and 2), co-existence of both strains (**Fig. 5c**, center, cluster 4), or low cell counts
333 of both strains (**Fig. 5c**, center, cluster 3). Representative images of droplets from each cluster
334 showed significant differences in community composition (**Fig. 5c**, right). A model of a
335 bidirectional negative interaction network displaying strong and weak negative interactions was
336 able to recapitulate the cell count distribution (**Fig. 5c**, middle, **Table S3**).

11

337   We next evaluated whether the model could recapitulate the cell count distributions of
338   networks that displayed positive interactions. Models constructed for the EC Met-, ST Lac*
339   consortium in two different environments exhibiting unidirectional or bidirectional positive
340   interactions (**Table 1**, E3-4) could recapitulate the cell count distributions (**Fig. 5d,e**). Next, a
341   model was developed for the mazF inhibition consortium (**Table 1**, E2) that displayed a
342   bidirectional negative interaction network. A model of strong and weak bidirectional negative
343   interactions represented the negative correlation in cell counts of the sender and receiver strains
344   (**Fig. 5f**). Our results demonstrate that bidirectional negative interaction networks can realize
345   distinct community state distributions (**Fig. 5c,f**). In the model, the number of partner cells required
346   to impact the probability of cell division dictates the strength of an interaction (**Fig. 5f**, **Fig. S7**).
347   The toxin mediated negative interaction in the mazF inhibition consortium (**Table 1**, E2) exhibited
348   a higher sensitivity to partner cell number than the negative interaction from ST Lac* to EC WT in
349   glucose minimal media (**Table 1**, E5, **Fig. S7**). Therefore, the recipients of the strong negative
350   interactions displayed different sensitivities to variations in donor cell number, providing insight
351   into the qualitative dissimilarities in the cell count distributions. In sum, the model was able to
352   describe the cell count distributions for positive and negative interactions mediated by distinct
353   molecular mechanisms, illustrating that a probabilistic growth model can explain the variability in
354   community states in small populations.
355
356
357

Fig. 5. Discrete-time Markov model of cell growth modified by microbial interactions can recapitulate cell count distributions in microfluidic droplets. (a) Schematic of variability in community assembly in small populations. Stochasticity in intracellular molecular concentrations can alter the strength of microbial interactions, generating different community states (high blue cells, low yellow cells or the reciprocal). **(b)** Schematic of the discrete-time Markov model of cell growth modified by microbial interactions. At each time step, each cell can undergo cell division, cell death or remain static according to the probabilities P_{div}, P_{death} or P_{static}, respectively. **(c)** Inferred network topology using MINI-Drop (left) for the EC WT, ST Lac* consortium in glucose minimal media (**Table 1**, E5). Node size and edge weight represent the average cell count of each strain grown in isolation and the interaction strength, respectively. Scatter plot of

369 experimentally measured cell counts (blue circles, n=257) of EC WT and ST Lac* or model steady-states
370 (red circles, n=200). This bidirectional negative interaction network generated qualitatively different
371 community compositions corresponding to (1) low and high EC WT and ST Lac*, respectively, (2) high EC
372 WT and ST Lac*, (3) low EC WT and ST Lac*, (4) high EC WT and low ST Lac*. Fluorescence microscopy
373 images (right) of a representative droplet in each community state 1-4 are shown (right). **(d)** Inferred network
374 for the EC Met-, ST Lac* consortium (top) in lactose minimal media supplemented with methionine (**Table
375 1**, E4). Scatter plot of experimentally measured cell counts (blue circles, n=118) of EC Met- and ST Lac* or
376 model steady-states (red circles, n=200). **(e)** Inferred interaction network for the EC Met-, ST Lac*
377 consortium in lactose minimal media (top, **Table 1**, E3). Scatter plot of experimentally measured cell counts
378 (blue circles, n=141) of EC Met- and ST Lac* or model steady-states (red circles, n=200). **(f)** Inferred
379 interaction network for the sender, receiver consortium (top, **Table 1**, E2). Scatter plot of experimentally
380 measured cell counts (blue circles, n=93) of the sender and receiver strains or model steady-states (red
381 circles, n=200).

382

Discussion

384 We showed that MINI-Drop can rapidly infer pairwise as well as higher-order microbial interactions
385 in 2- to 3-member consortia in different environmental conditions. This method can be scaled to
386 quantify interactions in higher-dimensional (>3 members) communities using compatible
387 fluorescent labels or combinatorial fluorescent imaging of multiple reporters within the same cell.
388 Combinatorial labeling via fluorescence in situ hybridization (Liu et al., 2011; Valm et al., 2012) or
389 fluorescent labeling of the bacterial outer membranes via biorthogonal click chemistry could be
390 used to measure the absolute abundance of organisms that are not genetically tractable (Geva-
391 Zatorsky et al., 2015).

392 In MINI-Drop, a single experiment generates hundreds to thousands of replicates of
393 unique sub-communities. The initial mean number of cells per drop can be manipulated to
394 investigate the contribution of initial cell density to microbial interactions or increase the proportion
395 of multi-strain droplets for interrogation of higher-order interactions. MINI-Drop does not require
396 coexistence of community members to determine interactions because fluorescently tagged
397 single cells encapsulated in a droplet can be accurately quantified.

398 Previous methods of microbial interaction inference using modeling frameworks such as
399 the generalized Lotka-Volterra (gLV) model are constrained by mathematical relationships
400 (Momeni et al., 2017). For example, a gLV model of strong bidirectional positive interactions tends
401 to be unstable, leading to potential underrepresentation of bidirectional positive interactions.
402 Further, it is challenging to pinpoint if the failure of a pairwise gLV model to accurately fit
403 experimental data is attributed to the presence of higher-order interactions or to unmodeled
404 dynamics such as metabolites mediating the interactions. By contrast, MINI-Drop is not
405 constrained to a defined mathematical framework and thus can rapidly identify higher-order
406 interactions in the networks. We showed that MINI-Drop accurately inferred diverse interaction
407 topologies including unidirectional positive, bidirectional positive or bidirectional negative
408 networks. In addition to deciphering engineered interactions, MINI-Drop illuminated unexpected
409 negative pairwise interactions and higher-order interactions in the networks. The unexpected
410 higher-order interaction that inhibited EC WT in the presence of both EC Met- and ST Lac* could
411 be explained by robust growth of the mutualistic pair EC Met- and ST Lac*, which in turn
412 negatively impacted EC WT. Across all experiments, *S. typhimurium* exhibited the strongest
413 outgoing negative interactions as well as the highest carrying capacity, suggesting that the
414 negative interactions could arise from competition for limited resources or space or the production
415 of toxic compounds.

14

416   The throughput of the MINI-Drop method was enabled by coupling two automated and
417   scalable technologies, droplet microfluidics and computational image analysis. The large number
418   of sub-community replicates provided by MINI-Drop allows investigation of the contribution of
419   initial conditions to community assembly in small populations. A probabilistic analysis of the
420   distribution of community states provides insight into the stochastic nature of microbial
421   interactions and impact of these parameters on community assembly. For example, we observed
422   that bidirectional positive networks displayed frequent co-occurrence (**Fig. 5e, Fig. S3, Fig. S4**)
423   whereas a bidirectional negative network can realize a set of distinct community states (**Fig. 5c,e**).
424   Our stochastic growth model can recapitulate the community states observed
425   experimentally a set of synthetic communities. This demonstrates that a simple probabilistic
426   representation of cell growth, death and microbial interactions can give rise to multiple community
427   steady-states from the same initial conditions. Our modeling framework could be used to predict
428   the probability of strain growth as a function of the initial strain proportions and cell density. These
429   parameters could be manipulated to maximize the likelihood of community member coexistence
430   in multi-species consortia. In sum, we developed a systematic procedure to elucidate microbial
431   interaction networks in microdroplets. Future work will apply MINI-Drop to study diverse cellular
432   interactions such as interkingdom or mammalian cell interactions.

433   **MATERIALS AND METHODS**
434

435   *Dynamic range of cell counting*
436   The bacterial strains EC Met- (CFP), EC WT (RFP), and ST Lac* (YFP) were grown in LB medium
437   to early stationary phase, centrifuged at 18,000xg for 1 min, decanted, and resuspended in M9
438   minimal medium without glucose. Next, the cells were centrifuged at 18,000xg for 1 min, decanted
439   and resuspended in a smaller volume of M9 minimal medium without glucose to concentrate the
440   cells. The OD600 values of the concentrated EC Met-, EC WT and ST Lac* cultures were 14.4,
441   19.6, and 6.4, respectively. Equal volumes of each culture were combined to generate the mixed
442   culture. The mixed culture was serially diluted by a factor of 2 until a dilution of 2^{-7} was reached.
443   The diluted cultures were encapsulated separately using the droplet maker device and the
444   resulting droplets were imaged and quantified using the computational image analysis pipeline.

445   *Bacterial cell culturing*
446   Strains were grown for approximately 12 hours at 37ºC in LB, diluted 1:50 into fresh LB, and then
447   grown to an OD600 of 0.3-1. Next, the culture (3 mL) was centrifuged for 2 min at 3,500 x g and
448   supernatant was removed. The cells were washed 4X by resuspending the pellet in 0.5 mL of
449   minimal media and centrifuged as described above. The cell cultures containing different strains
450   were normalized to an OD600 of 0.15 and mixed in a 1:1 ratio. In the mutualism experiment (E2),
451   *B. subtilis* and *E. coli* were mixed in a 2:1 volumetric ratio to account for differences in the cell
452   number to OD ratios. In experiment E1, cells were cultured in M9 supplemented with glucose (1X
453   M9 salts, 2 mM $MgSO_4$, 100 μM $CaCl_2$, 0.4% glucose) and 25 μg/mL chloramphenicol (Sigma).
454   In experiment E2, cells were cultured in LB media containing 50 ng/mL anhydrotetracycline (aTc,
455   Cayman Chemicals), 0.1% arabinose (Sigma) and 25 μg/mL chloramphenicol. In experiments E3-
456   E7, cells were cultured in M9 media (1X M9 salts, 2 mM $MgSO_4$, 100 μM $CaCl_2$) supplemented
457   with 0.4% glucose, 0.2% lactose and/or 200 μM methionine as indicated.

458

Number	Strains	Media	Figure
E1	BS Trp- EC Met- (RFP)	M9 Glucose	2a-d
E2	EC Sender EC Receiver	LB	2e-h
E3	EC Met- (CFP) ST Lac* EC WT	M9 Lactose	3a,e,i 4d,e
E4	EC Met- (CFP) ST Lac* EC WT	M9 Lactose + Met	3b,f,j
E5	EC Met- (CFP) ST Lac* EC WT	M9 Glucose	3c,g,k
E6	EC Met- (CFP) ST Lac* EC WT	M9 Glucose + Met	3d,h,l
E7	EC Met- (CFP) ST Lac* EC Met- Lac* (RFP)	M9 Lactose	4b,c

Table 1. Strains used in growth experiments.

Strain	Genotype	Plasmid	Fluorescent reporter	Abbreviation	Reference
B. subtilis	*B. subtilis 168, trpC2, cat, amyE::Pveg-gfp-spec*	None	GFP	BS Trp-	(Burkholder and Giles, 1947)
E. coli	E. coli BW25113 pheA::Kan	pOSV005	RFP	EC Met- Lac* and EC Met- (RFP)	(Baba et al., 2006)
E. coli	E. coli BW27783	pOSV022	GFP	Sender	(Khlebnikov et al., 2001)
E. coli	E. coli MG1655z1	pOSV151	RFP	Receiver	(Cox et al., 2007)
E. coli	E. coli K12 BW25113, ∆*metB att*::pLC280 [kan P_L'-cfp oriR6K]	None	CFP	EC Met- (CFP)	(Adamowicz et al., 2018)
S. typhimurium	LT2, *metA*(P35L) *met*	None	YFP	ST Lac*	(Adamowicz et al., 2018;

16

	J(16:IS10) *att*::p LC246 [kan P_L'-yfp oriR6K]				Douglas et al., 2016)
E. coli	E. coli BW25113 metA::Kan	pOSV006	RFP	EC WT	(Baba et al., 2006)

461 **Table 2.** Strains and media conditions for each experiment.

462

Fabrication of microfluidic devices

463

464 Photoresist masters of 25 µm layer height were fabricated by spinning a layer of photoresist SU-
465 8 3025 (Microchem) onto a silicon wafer (University Wafer), then baked at 95°C for 10 minutes.
466 Following baking, photoresist master was patterned by UV photolithography over a photomask
467 (**File S1**, CADArt). The master was subjected to post-exposure bake at 95°C for 4 min and
468 developed in fresh SU-8 developer (Microchem) for 6 min, prior to rinsing with isopropyl alcohol
469 (Fischer Scientific) and baking at 150°C to remove the solvent. The microfluidic devices were
470 fabricated by pouring poly(dimethylsiloxane) at a 11:1 polymer-to-crosslinker ratio (Dow Corning
471 Sylgard 184) onto the master and curing at 65ºC for 1 hr. The PDMS devices were excised with
472 a scalpel and cored with a 0.75 mm biopsy core (World Precision Instruments) to create inlets
473 and outlets. The device was then bonded to a microscope glass slide using O2 plasma cleaner
474 (Harrick Plasma), and channels were treated with Aquapel (PPG Industries) to render them
475 hydrophobic. Finally, the devices were baked at 65°C for 20 min to evaporate excess Aquapel
476 prior to use.

Encapsulation of cells into droplets and fluorescence microscopy

477

478 To encapsulate cells into droplets, 1 mL syringes (BD Luer Lok) were fitted with 27 gauge needles
479 and PE/2 tubing. 500 µL of the culture was loaded into a 1 mL syringe. Hydrofluoroether oil was
480 prepared with 2% Krytox as surfactant and loaded into a 1 mL syringe. The free end of the tubing
481 was primed and inserted into the droplet-making device. Droplets were generated using 600 µL
482 hr^{-1} oil and 300 µL hr^{-1} cell mixture flow rates at a 30 µm x 25 µm junction, which generated ~40
483 µm diameter droplets at 4.8 kHz. Droplets were collected into a 1.5 mL microfuge tube for 15 min
484 and incubated for 18 hr at 37ºC. Droplets were imaged using chamber microscopy slides
485 (Invitrogen C10228) and imaged with a 20X objective (Nikon, MRH10201) on a Ti-E Eclipse
486 inverted microscope (Nikon). Fluorescence was imaged using the following filters (Chroma): (1)
487 CFP: 436nm/20nm (ex), 480nm/40nm (em); (2) GFP: 470nm/40nm (ex), 525/50nm (em); (3) RFP:
488 560nm/40nm (ex), 630/70nm (em); and (4) YFP: 500nm/40nm (ex), 535nm/30nm (em).

Fluorescence microscopy image analysis

489

490 Custom code in Python was used for automated cell counting in droplets and microbial interaction
491 network inference. Droplets were identified from the phase contrast image using the Hough
492 transformation algorithm (OpenCV 3). Droplets with a diameter 10% larger or smaller than 40 µm
493 were removed from the dataset. Fluorescent cells were segmented by identifying connected
494 regions using the SimpleBlobDetector object (OpenCV 3). Droplets were binned by the presence
495 or absence of each fluorescently labeled strain. Interaction strength from strain *j* to strain *i*, where
496 droplet *d* contains d_k cells of strain *k*, was defined according to Equation 1. Network schematics
497 were drawn with Cytoscape 3.5 (Shannon et al., 2003).

498
$$log_2\left(\frac{mean(d_i \forall d | d_i > 0, d_j > 0)}{mean(d_i \forall d | d_i > 0, d_j = 0)}\right) \qquad (1)$$

499

500

501 *Discrete-time Markov model of cell growth*
502 A discrete-time Markov model was developed to recapitulate the experimentally measured cell
503 count distributions. At each time step, the propagation of each strain is determined by computing
504 the probability of cell division ($P_{div,i}$), cell death ($P_{death,i}$), and remaining unchanged ($P_{static,i}$)
505 (Equations 2-4).

$$P_{div,i} = r_{div,io} \times I_{ii}(n_i, s_{ii}, k_{ii}, a_{ii}) \times I_{ij}(n_j, s_{ij}, k_{ij}, a_{ij}) \qquad (2)$$

$$P_{death,i} = r_{death,io} \qquad (3)$$

$$P_{static,i} = 1 - (P_{div,i} + P_{death,i}) \qquad (4)$$

510 The parameter $r_{div,io}$ is the basal probability of cell division for strain *i*. The parameter $r_{death,io}$
511 represents the probability of cell death of strain *i* (constant). n_i denotes the number of cells of
512 strain *I* and s_{ij} defines whether the outgoing interaction of strain *j* (donor) to strain *i* is positive
513 ($s_{ij} = 1$) or negative ($s_{ij} = -1$). The parameters k_{ij} and a_{ij} define the sigmoidal interaction
514 function I_{ij}, representing the incoming interaction for strain *i* produced by strain *j* (Equation 5).

$$I_{ij} = \begin{cases} \frac{(1+a_{ij})e^{k_{ij}n_j}}{1+a_{ij}e^{k_{ij}n_j}}, & if\ s_{ij} = +1 \\ \frac{(1+a_{ij})}{1+a_{ij}e^{k_{ij}n_j}}, & if\ s_{ij} = -1 \end{cases} \qquad (5)$$

516 The negative interaction function approaches zero as a function of n_j whereas the positive
517 interaction approaches $(1 + a_{ij})/a_{ij}$ as a function of n_j. The values of a_{ij} and $r_{div,i}$ are constrained
518 such that $P_{div,i} \leq 1$ (Equation 6). The self-interaction function $I_{ii}(n_i, s_{ii}, k_{ii}, a_{ii})$ is less than one
519 ($s_{ii} = -1$) and approaches zero as a function of n_i, leading to saturation of the number of cells of
520 strain *i*. The interaction function I_{ij}, is equal to 1 when $n_j = 0$, representing the absence of an
521 interaction between strain *i* and *j*. In the absence of an interaction between strain *i* and *j*, $P_{div,i}$ is
522 not dependent on strain *j* $(s_{ij} = -1, k_{ij} = 0, a_{ij} = 0)$. The outgoing interaction from the partner
523 strain *j* $I_{ij}(n_j, s_{ij}, k_{ij}, a_{ij})$ can be positive or negative depending on the value of the parameter s_{ij}.
524 The parameters a_{ij} and k_{ij} determine the interaction sensitivity defined as the number of partner
525 cells at the half-maximum of the interaction function $\hat{n}_j$. The parameters

$$\hat{n}_j = \frac{1}{k_{ij}} \ln \left(\frac{1}{a_{ij}} + 2\right) \qquad (6)$$

$$\left. \frac{dI_{ij}}{dn_j} \right|_{\hat{n}_j} = \begin{cases} \frac{k_{ij}(\frac{1}{a_{ij}}+2)}{4(a_{ij}+1)}, & if\ s_{ij} = 1 \\ \frac{-k_{ij}(\frac{1}{a_{ij}}+2)a_{ij}}{4(a_{ij}+1)}, & if\ s_{ij} = -1 \end{cases} \qquad (7)$$

528 At each time step, the state transition of a cell is independent of all other cells and the cell's prior
529 history. The state transitions were simulated by sampling from a trinomial distribution determined
530 by the probabilities $P_{div,i}$, $P_{death,i}$, and $P_{static,i}$. Communities were simulated for 100 time-steps
531 wherein each time-step corresponded to 10.8 minutes of experimental time. Variables were
532 constrained such that the cell populations reached a steady state within the simulation time. The
533 initial condition for all simulations was $n_i, n_j = 1$. Model parameters are listed in **Table S3**.
534

18

542 **AUTHOR CONTRIBUTIONS**
543 O.S.V., R.H.H. and P.A.R. designed the research. R.H.H., J.W.T., R.L.C. carried out the
544 experiments. R.H.H. designed and implemented data analysis methods and computational
545 modeling. R.H.H., R.L.C. and O.S.V. wrote the manuscript and J.W.T. assisted in revising the
546 manuscript.
547

548 **CONFLICT OF INTEREST**
549 The authors do not have a conflict of interest.
550

551 **REFERENCES**
552 Adamowicz, E.M., Flynn, J., Hunter, R.C., and Harcombe, W.R. (2018). Cross-feeding
553 modulates antibiotic tolerance in bacterial communities. ISME J. 1–13.

554 Baba, T., Ara, T., Hasegawa, M., Takai, Y., Okumura, Y., Baba, M., Datsenko, K.A., Tomita, M.,
555 Wanner, B.L., and Mori, H. (2006). Construction of Escherichia coli K-12 in-frame, single-gene
556 knockout mutants: The Keio collection. Mol. Syst. Biol. *2*.

557 Bachmann, H., Fischlechner, M., Rabbers, I., Barfa, N., Branco dos Santos, F., Molenaar, D.,
558 and Teusink, B. (2013). Availability of public goods shapes the evolution of competing metabolic
559 strategies. Proc. Natl. Acad. Sci. *110*, 14302–14307.

560 Bairey, E., Kelsic, E.D., and Kishony, R. (2016). High-order species interactions shape
561 ecosystem diversity. Nat. Publ. Gr. *7*, 1–7.

562 Berendsen, R.L., Pieterse, C.M.J., and Bakker, P.A.H.M. (2012). The rhizosphere microbiome
563 and plant health. Trends Plant Sci.

564 Boedicker, J.Q., Vincent, M.E., and Ismagilov, R.F. (2009). Microfluidic Confinement of Single
565 Cells of Bacteria in Small Volumes Initiates High-Density Behavior of Quorum Sensing and
566 Growth and Reveals Its Variability **. Angew. Chemie *48*, 5908–5911.

567 von Bronk, B., Schaffer, S.A., Götz, A., and Opitz, M. (2017). Effects of stochasticity and
568 division of labor in toxin production on two-strain bacterial competition in Escherichia coli. PLoS
569 Biol.

570 Burkholder, P., and Giles, N. (1947). Induced Biochemical Mutations in Bacillus subtilis. Am. J.
571 Bot. *34*, 345–348.

572 Cao, H.T., Gibson, T.E., Bashan, A., and Liu, Y.Y. (2017). Inferring human microbial dynamics
573 from temporal metagenomics data: Pitfalls and lessons. BioEssays *39*, 1–12.

574 Cao, X., Hamilton, J.J., and Venturelli, O.S. (2018). Understanding and Engineering Distributed
575 Biochemical Pathways in Microbial Communities Biochemistry XXXX, XXX, XXX−XXX. *17*, 28.

576 Clemente, J.C., Ursell, L.K., Parfrey, L.W., and Knight, R. (2012). The impact of the gut
577 microbiota on human health: An integrative view. Cell.

578 Connell, J.L., Kim, J., Shear, J.B., Bard, A.J., and Whiteley, M. (2014). Real-time monitoring of

579 quorum sensing in 3D-printed bacterial aggregates using scanning electrochemical microscopy.
580 Proc. Natl. Acad. Sci. *111*, 18255–18260.

581 Cox, R.S., Surette, M.G., and Elowitz, M.B. (2007). Programming gene expression with
582 combinatorial promoters. Mol. Syst. Biol. *3*.

583 Douglas, S.M., Chubiz, L.M., Harcombe, W.R., Ytreberg, F.M., and Marx, C.J. (2016). Parallel
584 mutations result in a wide range of cooperation and community consequences in a two-species
585 bacterial consortium. PLoS One *11*, 1–19.

586 Fisher, C.K., and Mehta, P. (2014). Identifying keystone species in the human gut microbiome
587 from metagenomic timeseries using sparse linear regression. PLoS One *9*, 1–10.

588 Friedman, J., Higgins, L.M., and Gore, J. (2017). Community structure follows simple assembly
589 rules in microbial microcosms. Nat. Ecol. Evol. *1*.

590 Geva-Zatorsky, N., Alvarez, D., Hudak, J.E., Reading, N.C., Erturk-Hasdemir, D., Dasgupta, S.,
591 Von Andrian, U.H., and Kasper, D.L. (2015). In vivo imaging and tracking of host-microbiota
592 interactions via metabolic labeling of gut anaerobic bacteria. Nat. Med. *21*, 1091–1100.

593 Guo, X., and Boedicker, J.Q. (2016). The contribution of high-order metabolic interactions to the
594 global activity of a four-species microbial community. PLoS Comput. Biol. *12*, 1–13.

595 Guo, M.T., Rotem, A., Heyman, J.A., and D. A. Weitz (2012). Droplet microfluidics for high-
596 throughput biological assays. Lab Chip *12*, 2146–2155.

597 Hansen, R.H., Timm, A.C., Timm, C.M., Bible, A.N., Pelletier, D.A., Simpson, M.L., and Doktycz,
598 M.J. (2016). Stochastic Assembly of Bacteria in Microwell Arrays Reveals the Importance of
599 Confinement in Community Development. 1–18.

600 Harcombe, W.R. (2010). Novel cooperation experimentally evolved between species. Evolution
601 (N. Y). *64*, 2166–2172.

602 Harcombe, W.R., Betts, A., Shapiro, J.W., and Marx, C.J. (2016). Adding biotic complexity alters
603 the metabolic benefits of mutualism. Evolution *70*, 1871–1881.

604 Horowitz, J., Normand, M.D., Corradini, M.G., and Peleg, M. (2010). Probabilistic model of
605 microbial cell growth, division, and mortality. Appl. Environ. Microbiol. *76*, 230–242.

606 Khlebnikov, A., Datsenko, K.A., Skaug, T., Wanner, B.L., and Keasling, J.D. (2001).
607 Homogeneous expression of the PBADpromoter in Escherichia coli by constitutive expression of
608 the low-affinity high-capacity araE transporter. Microbiology *147*, 3241–3247.

609 Kong, W., Meldgin, D.R., Collins, J.J., and Lu, T. (2018). Designing microbial consortia with
610 defined social interactions. Nat. Chem. Biol. *14*, 821–829.

611 Liu, A., Archer, A.M., Biggs, M.B., and Papin, J.A. (2017). Growth-altering microbial interactions
612 are responsive to chemical context. PLoS One *12*, e0164919.

613 Liu, P., Meagher, R.J., Light, Y.K., Yilmaz, S., Chakraborty, R., Arkin, A.P., Hazen, T.C., and
614 Singh, A.K. (2011). Microfluidic fluorescence in situ hybridization and flow cytometry
615 (μFlowFISH). Lab Chip *11*, 2673–2679.

616 Momeni, B., Xie, L., and Shou, W. (2017). Lotka-Volterra pairwise modeling fails to capture
617 diverse pairwise microbial interactions. Elife *6*, 1–34.

618 Mounier, J., Monnet, C., Vallaeys, T., Arditi, R., Sarthou, A.-S., Hélias, A., and Irlinger, F.

619   (2008). Microbial interactions within a cheese microbial community. Appl. Environ. Microbiol. *74*,
620   172–181.

621   Park, J., Kerner, A., Burns, M.A., and Lin, X.N. (2011). Microdroplet-Enabled Highly Parallel Co-
622   Cultivation of Microbial Communities. PLoS One *6*.

623   Sender, R., Fuchs, S., and Milo, R. (2016). Revised Estimates for the Number of Human and
624   Bacteria Cells in the Body. PLoS Biol.

625   Shannon, P., Markiel, A., Ozier, O., Baliga, N., Wang, J., Ramage, D., Amin, N., Schwikowski, B.,
626   and Ideker, T. (2003). Cytoscape: A Software Environment for Integrated Models of
627   Biomolecular Interaction Networks. Genome Res. 426.

628   Society, E. (2015). Higher Order Interactions in Ecological Communities : What Are They and
629   How Can They be Detected ? Author (s): Ian Billick and Ted J . Case Published by : Ecological
630   Society of America HIGHER ORDER INTERACTIONS IN ECOLOGICAL COMMUNITIES :
631   WHAT ARE THEY . *75*, 1529–1543.

632   Stoodley, P., Wilson, S., Hall-Stoodley, L., Boyle, J.D., Lappin-Scott, H.M., and Costerton, J.W.
633   (2001). Growth and Detachment of Cell Clusters from Mature Mixed-Species Biofilms. Appl.
634   Environ. Microbiol. *67*, 5608–5613.

635   Valm, A.M., Mark Welch, J.L., and Borisy, G.G. (2012). CLASI-FISH: Principles of combinatorial
636   labeling and spectral imaging. Syst. Appl. Microbiol. *35*, 496–502.

637   Vega, N.M., and Gore, J. (2017). Stochastic assembly produces heterogeneous communities in
638   the Caenorhabditis elegans intestine. PLoS Biol.

639   Venturelli, O.S., Egbert, R.G., and Arkin, A.P. (2016). Towards engineering biological systems
640   in a broader context. J. Mol. Biol. *428*, 928–944.

641   Venturelli, O.S., Tei, M., Bauer, S., Chan, L.J.G., Petzold, C.J., and Arkin, A.P. (2017).
642   Programming mRNA decay to modulate synthetic circuit resource allocation. Nat. Commun. *8*.

643   Venturelli, O.S., Carr, A., Fisher, G., Hsu, R., Lau, R., Bowen, B.P., Hromada, S., Northen, T.,
644   and Arkin, A.P. (2018). Deciphering microbial interactions in synthetic human gut microbiome
645   communities. Mol. Syst. Biol. *14*, e8157.

646   Zhou, J., Liu, W., Deng, Y., Jiang, Y.H., Xue, K., He, Z., Van Nostrand, J.D., Wu, L., Yang, Y.,
647   and Wang, A. (2013). Stochastic assembly leads to alternative communities with distinct
648   functions in a bioreactor microbial community. MBio.